Stability analysis of TJ-II stellarator NBI driven Alfvén Eigenmodes in ECRH and ECCD experiments

Á. Cappa[1], **J. Varela**[2], **D. López Bruna**[1], **E. Ascasíbar**[1]
M. Liniers[1], **L.G. Eliseev**[3], **J.M. Fontdecaba**[1]
J.M. García-Regaña[1], **A. González-Jerez**[1]
N.K. Kharchev[3,4], **F. Medina**[1], **A.V. Melnikov**[3,5,6]
S. Mulas[1], **M. Ochando**[1], **D. Spong**[7]
J.L. Velasco[1] **and TJ–II Team**

[1] Laboratorio Nacional de Fusión–CIEMAT, Madrid, Spain
[2] National Institute for Fusion Science, Toki, Japan
[3] National Research Center "Kurchatov Institute", Moscow, Russia
[4] Prokhorov General Physics Institute of the Russian Academy of Sciences, Moscow, Russia
[5] National Nuclear Research University 'MEPhI', Moscow, Russia
[6] Moscow Institute of Physics and Technology, Dolgoprudny, Russia
[7] Oak Ridge National Laboratory, Oak Ridge, USA

E-mail: `alvaro.cappa@ciemat.es`

November 2020

Abstract. In this paper, we analyze the impact of Electron Cyclotron Resonance Heating (ECRH) and Electron Cyclotron Current Drive (ECCD) on the Alfvénic instabilities driven by Neutral Beam Injection (NBI) observed in the TJ-II stellarator. An MHD stability analysis of driven Alfvén Eigenmodes (AEs) compatible with the experimental plasma parameters is carried out in order to compare with the data provided by magnetic coils, radiation monitors, and heavy ion beam probes. To this end, the vacuum magnetic configuration modified by the different levels of plasma current, the thermal plasma parameters and the fast ion pressure profiles generated by the co-injected neutral beam, are entered in the FAR3d gyro-fluid code in order to follow the linear evolution of the destabilized plasma equilibrium. Linear growth rates and radial location of the dominant predicted modes coincident in frequency with the observed fluctuations are presented. Despite the uncertainties related to the estimation of the rotational transform profile, the code predictions agree within reasonable accuracy with the experimental results.

1. Introduction

Controlling the amplitude of Alfvén Eigenmodes (AEs) in fusion plasmas is an open issue with essential relevance for ITER and beyond, because the fast ion losses associated with these modes might be deleterious for plasma performance and heating efficiency, as well as destructive for the plasma facing components. Several actuators, whose impact has been clearly demonstrated in tokamaks [1–5] and in stellarators [6–8], are presently being considered for this purpose. Reference [9] provides an overview of such methods and their underlying mechanisms related to AE physics.

Alfvén Eigenmodes driven by Neutral Beam Injection (NBI) are found in several magnetic configurations of the TJ–II stellarator [10–12], providing the opportunity to test control knobs that may modify, or eventually suppress, the Alfvén activity of the device. In this context, considerable effort has been devoted to investigate the impact of ECRH and ECCD on AEs in TJ-II plasmas. Experiments exploring other actuators, as NBI injection energy, magnetic configuration [13, 14], ohmic current induction or pellet injection have also been addressed but the clearest influence, keeping the minimum impact on the plasma and magnetic configuration parameters, has been obtained using ECCD as actuator. Describing the results of these experiments is one of the primary motivations of the paper. The other main goal, much more ambitious, is to reproduce the experimental results using Alfvén continuum calculations performed with the STELLGAP code and linear MHD simulations to estimate the growth rate and radial structure of the dominant AEs by means of the gyro-fluid FAR3d code.

The paper is structured as follows; we first present a simple estimation, based on the cylindrical shear Alfvén continuum calculated for the main TJ-II parameters, that allows us to determine the type of gap modes that can be destabilized below 500 kHz, the typical frequency range in which NBI driven Alfvén instabilities are detected in TJ-II; then, the device heating systems and the relevant diagnostics for this work are briefly described; section 4 focuses on the description of the experimental results for all the heating scenarios considered while sections 5 and 6 present the calculation of the fast-ions and rotational transform profiles associated to these scenarios; section 7 is devoted to the shear Alfvén spectrum calculations with STELLGAP and the FAR3d linear stability analysis for the aforementioned conditions; finally, we come to the conclusions.

2. Shear Alfvén gap modes in the TJ–II stellarator

The TJ–II device is a four-period ($N_f = 4$) heliac type stellarator with low negative vacuum magnetic shear. The major and averaged plasma radii of the device are $R_0 = 1.5$ m and $\langle a \rangle \leq 0.22$ m respectively. The central magnetic field strength is 0.95 T (at the ECRH injection location) and a wide range of central rotational transform $\iota\!\!\!-(0)$ is achievable ($0.9 \leq |\iota\!\!\!-(0)| \leq 2.2$). For these parameters, we may determine approximately the typical frequencies of the shear Alfvén modes that can be excited within the gaps that appear in the continuum spectrum because of the periodicities in the magnetic field structure. The radial dependence of gap modes frequency on the rotational transform can be estimated using the cylindrical approximation for the longitudinal wave vector of a given m, n perturbation, usually written as [15]

$$k_{\|}(\rho) = (m\iota\!\!\!-(\rho) - n)/R_0, \tag{1}$$

where R_0 is the major radius of the device and m and n are the perturbation poloidal and toroidal mode numbers respectively. Following [16], we may calculate the characteristic gap "frequency" as

$$\omega_A(\rho) = |k^{\mu\nu}(\rho)| v_A(\rho), \tag{2}$$

where the quantity $k^{\mu\nu}(\rho)$ is given by

$$k^{\mu\nu}(\rho) = (\mu\iota\!\!\!-(\rho) - \nu N_f)/2R_0), \tag{3}$$

and $v_A(\rho) = B(\rho)/(\mu_0 \sum_i n_i(\rho) m_i)^{1/2}$ is the Alfvén velocity, that depends on the magnetic field (B) and the density (n_i) and mass (m_i) of the different plasma species. The parameters μ, ν label the Fourier expansion coefficients in Boozer coordinates, $\epsilon_B^{\mu\nu}(\rho)$ and $\epsilon_g^{\mu\nu}(\rho)$, of the magnetic field and the contravariant component of the metric tensor respectively. Each periodic component of the Fourier expansion creates a gap in the continuum, whose width depends on the magnitudes of $\epsilon_B^{\mu\nu}(\rho)$ and $\epsilon_g^{\mu\nu}(\rho)$ [17]. In eq. (3), instead of using ρ as independent variable, we may use the rotational transform itself and calculate $\omega_A(\iota\!\!\!-)$ for the range of $\iota\!\!\!-$ values characteristic of the magnetic configuration used in the experiments described in section 4, including the deviations from the equilibrium values induced by plasma current. Figure 1 shows the typical frequencies of gap modes associated to the dominant low order contributions to the Fourier expansion, i.e. TAE ($\mu = 1, \nu = 0$), HAE$_{21}$ ($\mu = 2, \nu = 1$) and HAE$_{31}$ ($\mu = 3, \nu = 1$), in the frequency range of interest. Other low order gaps, as HAE$_{11}$ ($\mu = 1, \nu = 1$), EAE ($\mu = 2, \nu = 0$) or NAE ($\mu = 3, \nu = 0$), appear much higher in frequency and are not seen in the figure. Deuterium ions for a given range of central densities ($n_i = 0.8 - 1.2 \times 10^{19}$ m^{-3}) and constant field $B = 0.95$ T have been taken to evaluate v_A.

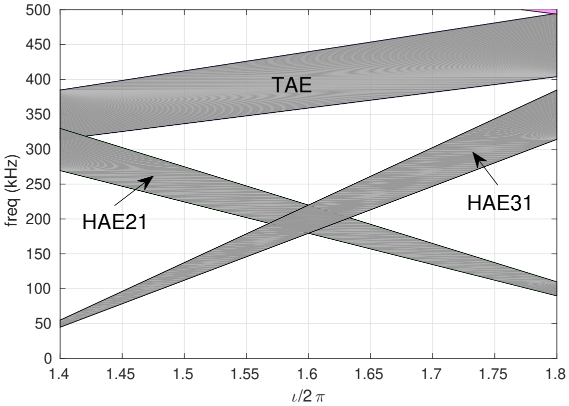

Figure 1. Typical frequencies of shear Alfvén gap modes for the range of rotational transform values found in the TJ-II standard magnetic configuration. The width of each gray-shaded band is only related to the range of different densities considered in the calculation. No estimation of the gap width related to the amplitudes of the $\epsilon_B^{\mu\nu}$ and $\epsilon_g^{\mu\nu}$ coefficients is considered here.

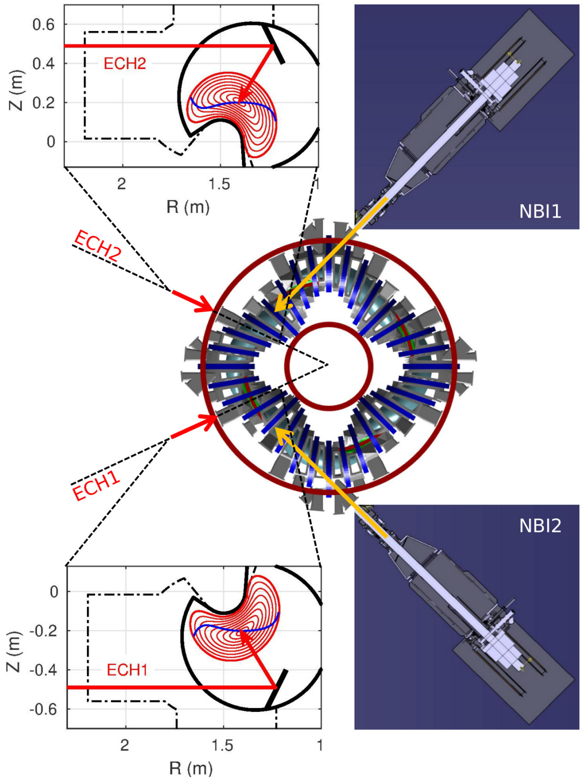

Figure 2. TJ-II stellarator heating systems. The last mirror of each ECRH transmission line is steerable. Both are located inside the vessel at stellarator symmetric positions. Neutral beams sources launch their beams parallel and anti-parallel to the magnetic field direction, which is mainly counter-clockwise when looking from above. NBI1 is the co-injector.

3. TJ–II stellarator and experimental set-up

TJ-II plasmas are created and heated by ECRH, NBI or a combination of both. The NBI heating system consists of two injectors, each providing up to 700 kW of co and counter sub-Alfvénic H$_0$ beams ($v_{beam}/v_A \sim 0.3 - 0.5$ for line averaged densities around $0.5 - 1.0 \times 10^{19}$ cm^{-3}) with ion source currents up to 60 A and with a maximum acceleration voltage of 34 kV. As corresponds to tangential injection (see figure 2), a high fraction of the fast ions have passing trajectories with a pitch ($\xi = v_\parallel/v$) distribution of the born ions strongly peaked around $\xi = 1$ [18]. The experiments described in this paper were carried out on mixed-fuel plasmas of deuterium (puffing) and hydrogen (NBI) using only the co-direction NBI1 injector. Consequently, the NBCD contribution to the total plasma current must be taken into account. Additionally, two 53.2 GHz gyrotrons, each of them generating up to 250 kW of EC power, heat the plasma using second harmonic X–mode. The power of each gyrotron is guided towards the vacuum vessel by its corresponding quasi-optical transmission line. Two internal steerable mirrors, one for each ECH beam (ECH1 and ECH2) allow us to scan the plasma toroidally and poloidally. The lines are located in stellarator symmetric positions ensuring in principle EC driven current compensation when launching parameters in both lines are equivalent. The heating systems and their power injection geometry are illustrated in figure 2.

Two heavy ion beam probes (HIBP), located at equivalent toroidal positions in different sectors of the device, simultaneously provide local measurements of plasma electric potential, density profile and poloidal magnetic field [19]. The size of their beam sample volume determines the spatial resolution of each diagnostic (1 cm). The radial position of the sampling volume ρ_{sv} can be swept over the plasma column $-1 < \rho_{sv} < 1$ several times during one single shot ($\sim$15 ms per sweep) allowing for profile measurement as long as steady state conditions are achieved. Negative and positive values of ρ_{sv} indicate high and low field side measurements respectively. Additionally, a 16-channel silicon photodiodes array (figure 3) providing line-integrated measurements of plasma radiation in the 2 eV-5 keV range helps determine the radial extension of the detected modes, as long as they have a clear impact on radiation. Unfortunately, the array of 25 Mirnov coils, used to measure the poloidal mode number of the perturbations, was not available when the experiment took place.

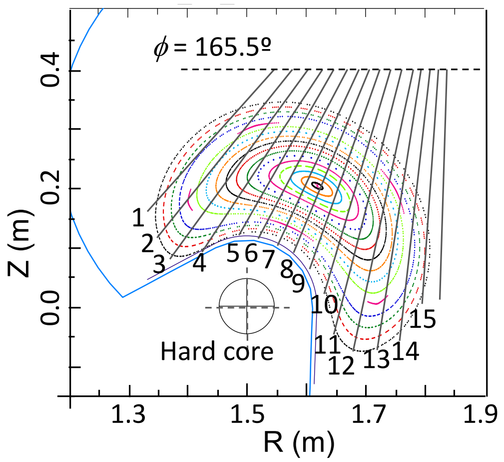

Figure 3. Radiation measurement set-up. The viewing lines of the 16 detectors are shown.

4. Experimental observations

4.1. NBI Plasmas

Figure 4 shows the time histories of total ECRH and co-NBI heating power, line-averaged electron density, central electron and ion temperatures (measured with ECE and NPA diagnostics respectively) and plasma current, for discharge #44257, in which several MHD instabilites appear during the NBI phase ($t \geq 1150$ ms). Injected power is 480 kW during the ECRH phase and 500 kW during the NBI phase. In this operation scheme, ECRH is switched-off at $t = 1150$ ms since it is mainly used to build the NBI target plasma. Central ECE temperature appears overestimated during the ECRH phase ($t = 1060 - 1150$ ms) because of the low density of the discharge. In these conditions, kinetic effects derived from highly focused ECRH beams (deviations from Maxwellian electron distribution function) and low optical plasma thickness prevent reliable ECE measurements. ECE temperature is routinely calibrated using the Thomson scattering profiles but this calibration is only valid for central channels and medium density conditions as the ones achieved in the NBI phase ($n_e \gtrsim 0.5 \times 10^{19}$ m^{-3}). The fast density ramp-up at $t = 1150$ ms is triggered by the switch-off of the ECRH power. ECRH pump-out effect disappear and the sudden cooling of the plasma eases the penetration of the surrounding neutrals. In addition, this fast increase in plasma density improves the NBI coupling and its heating efficiency. The NBI direct contribution to the particle source approximately doubles after ECRH switch-off, but still remains smaller than the other contributions such as recycling of shine-through (58%) or CX neutrals [20].

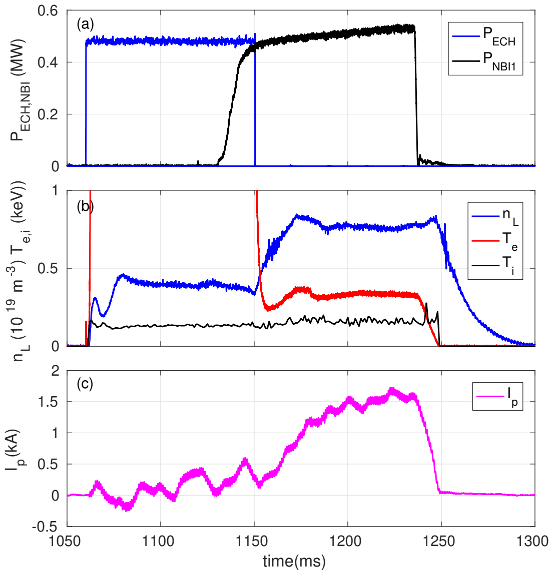

Figure 4. Time evolution of total heating power $P_{ECH} = P_{ECH1} + P_{ECH2} = 480$ kW and $P_{NBI} = 500$ kW (a), electron line density n_L and central electron/ion temperatures (b) and plasma current (c) in a shot with separate ECRH and NBI phases. Plasma current is stabilized around $t = 1200$ ms. The ordinates scale in (b) is chosen to clearly show the NBI phase time traces, even though it implies that electron temperature during ECRH phase goes off scale.

Plasma current driven by the co-NBI beam increases up to $I_p \approx 1.5$ kA and appears stable during the last 40 ms of the discharge. Current stabilization time is consistent with the L/R time, defined as $\tau_{LR} \simeq \sigma_{\parallel} \langle a \rangle^2 (\mu_0/2) \ln(8R_0/\langle a \rangle \mathrm{e}^{7/4})$, which calculated for the typical NBI plasma electron temperature yields $\tau_{LR} \approx 150$ ms. A surface average temperature using the $T_e(\rho)$ profile shown in figure 10 is considered in the calculation of the parallel conductivity $\sigma_{\parallel}$ [21]. A ratio $n_D/n_H \approx 1.8$, produced by the combination of deuterium gas puffed inside the device and the hydrogen NBI, is measured in this type of shot [22].

Figure 5 shows the spectrograms of the magnetic field fluctuations $\tilde{B}(t)$ (mainly the fluctuations in the poloidal component of $\mathbf{B}$) detected during the NBI phase by two Mirnov coils (MIR5C and MID5P13) located approximately 4 and 10 cm away from the LCFS at different toroidal and poloidal locations. Several low ($f \lesssim 100$ kHz) and high ($f > 100$ kHz) frequency instabilities are observed. The frequency of the most intense high frequency modes (1150 ms $<$ t $<$ 1175 ms) clearly shows the typical inverse square root dependence on plasma density characteristic of shear Alfvén waves. Although all the instabilities are detected by both magnetic coils, the amplitude of the induced perturbations depends on the coil location.

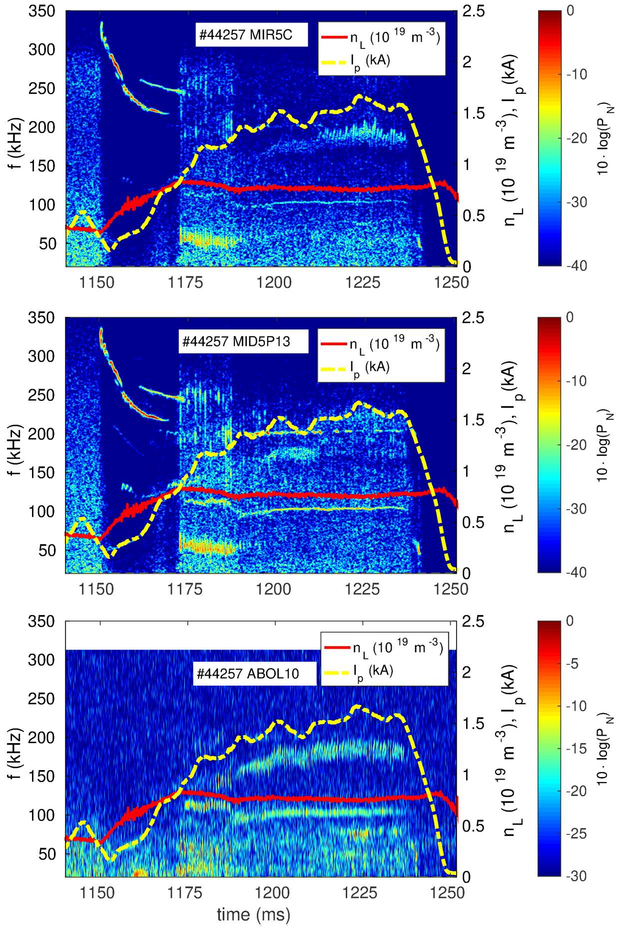

Figure 5. Top and middle panels show the magnetic fluctuations spectrograms obtained during the NBI phase ($t >$ 1150 ms), measured by two magnetic coils at different toroidal locations. Bottom panel shows the spectrogram of plasma radiation. Plasma current (yellow dashed line) and line density (red solid line) are also plotted.

Figure 5 also shows the spectrogram of the radiation detector looking towards the plasma core (labeled “10” in figure 3). The strong high-frequency perturbations (f $>$ 200 kHz) detected in magnetic field during the density ramp-up phase have no measurable impact on plasma radiation while the rest of instabilities detected for $t > 1170$ ms influence both magnetic and radiation behavior.

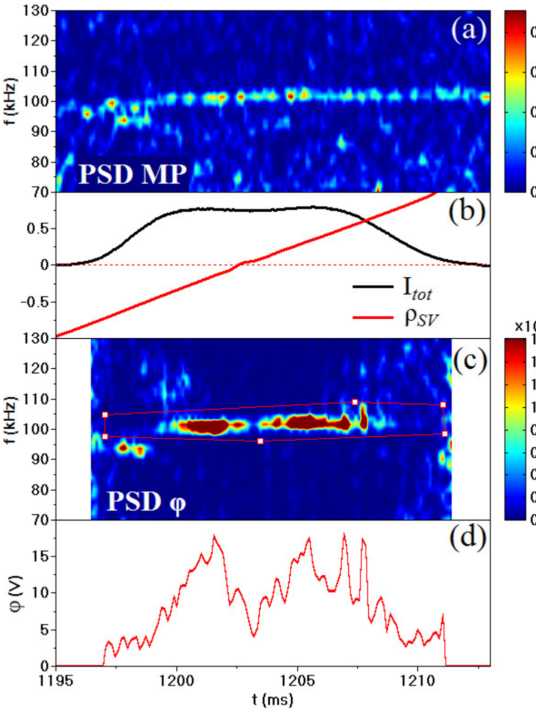

Figure 6. (a) Magnetic fluctuations measured by Mirnov coil during the HIBP2 scanning time interval. In (b), the HIBP2 secondary beam intensity $I_{tot}(t)$, proportional to plasma density, and the position of the heavy ion beam-plasma interaction volume, $\rho_{sv}(t)$ are plotted. The spectrogram of the electric potential fluctuations appears in (c) and the amplitude of these fluctuations as a function of time is shown in (d). Combining (b) and (d) we may find the radial structure of the perturbation (see figure 7).

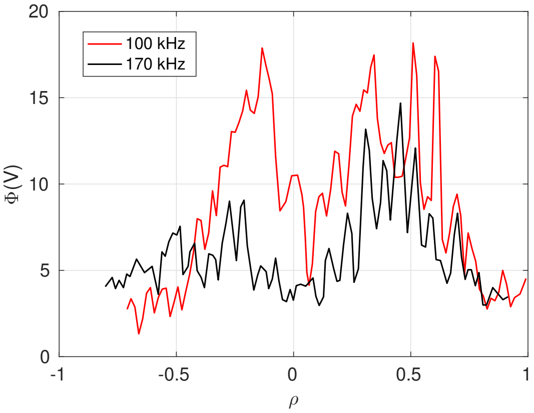

Figure 7. Radial structure of the electric potential perturbations measured by HIBP2 for the steady (red) and chirping modes (black) observed at $f \approx 100$ kHz and $f \approx 170$ kHz.

The two heavy ion beam probes (HIBP1 and HIBP2) were repeatedly scanning the plasma column during the discharge. For the shot represented in figure 4, two complete scans with both probes were performed at the beginning of the NBI phase, and two in the stationary phase between $t = 1195$ ms and $t = 1235$ ms, enabling the determination of the plasma potential perturbations associated to the most intense modes that are observed in these phases. Figure 6 shows an example of this type of measurement, obtained in one of the scans using HIBP2, for the mode that appears at $f \approx 100$ kHz. Assuming steady state conditions, the moving heavy ion beam provides the average amplitude of the perturbation as a function of time. Knowing the dependence of the probing beam position on time, the radial structure of the potential perturbation may be inferred. Figure 7 shows the perturbed potential profiles of the almost steady mode detected at 100 kHz and the chirping mode that appears around 170 kHz. Both perturbed potential profiles measured by HIBP1 and HIBP2 are compared in figure 8 showing a good agreement and confirming the expected toroidal extension of the 100 kHz Alfvén mode.

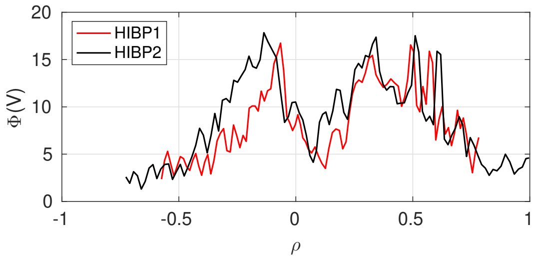

Figure 8. Radial structure of the 100 kHz electric potential perturbations measured by HIBP1 and HIBP2.

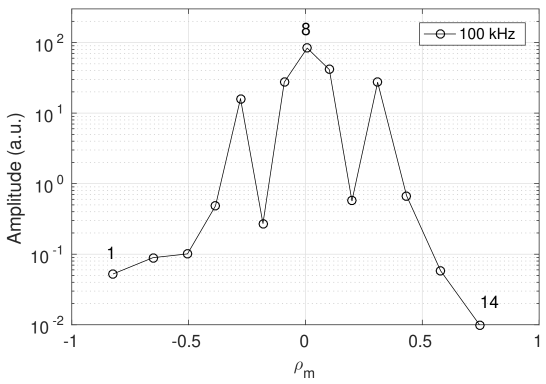

Figure 9. Amplitude of line integrated plasma radiation oscillations detected at $f \approx 100$ kHz. Minimum ρ_m corresponds to channel 1 according to the numbering shown in figure 3. Central (#8) and edge channels are indicated.

For comparison with the radial extension of the 100 kHz mode detected by both heavy ion beam probes, the amplitude of line integrated plasma radiation perturbations measured by the array of photodiodes at this same frequency is shown in figure 9. The values of the ρ_m coordinate associated to each channel actually correspond to the lower value of ρ encountered along the line of sight of each detector (see figure 3). The radial extension of the perturbations in plasma radiation ($-0.5 < \rho_m < +0.5$) is consistent with the potential profiles measured by HIBP's. Electron temperature and density profiles measured by Thomson scattering at $t = 1200$ ms are shown in figure 10. Although no measurement of the T_i profile is available, a reasonable estimate in NBI plasmas can be obtained by taking $T_i(\rho)$ proportional to the electron temperature profile and using the central ion temperature provided by NPA [23]. The ion density profile consistent with the Z_{eff} profile is also shown.

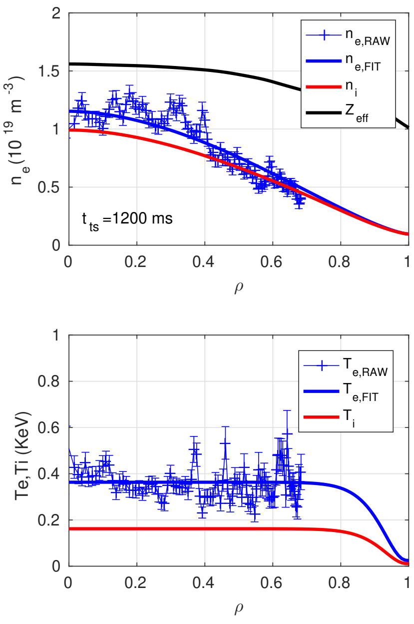

Figure 10. Electron/ion density and temperature profiles of the NBI heated plasma. Profiles were measured at $t = 1200$ ms.

4.2. NBI+ECRH/ECCD Plasmas

Starting from the NBI scenario described above, we may first study the effect produced on the plasma parameters, and also on the AEs activity, when on-axis ECRH power is added during the NBI phase. To this end, only one of the ECH beams is switched on again at $t = 1170$ ms. Initial ECRH power remains the same as in the reference scenario (around 480 kW) while only 240 kW, corresponding to ECH1 (or ECH2), is applied during the second phase. Changing the injection angle of one of the ECH beams from $N_{\parallel} = 0.0$ to $N_{\parallel} = +0.2$ allows us to induce on-axis current (counter-ECCD) with minor changes in the beam power deposition profile. By comparing shots with and without ECCD we may investigate the influence

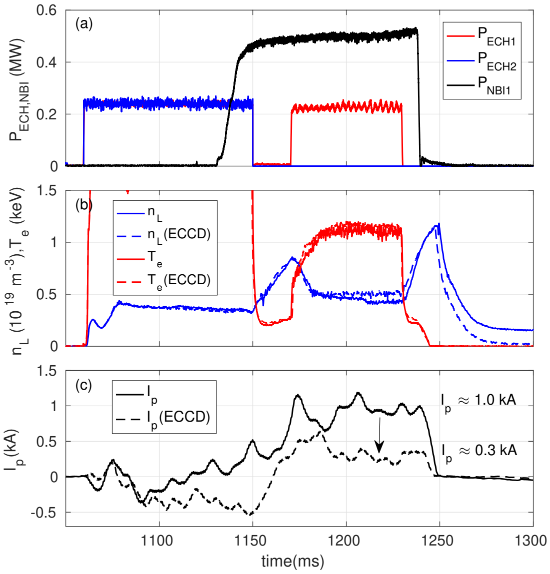

Figure 11. Heating power (a), line density n_L, central electron temperature (b) and plasma current (c) in two shots with four separate phases: ECH1+ECH2, NBI, NBI+ECH1 and NBI again. The figure compares a shot with ECCD (dashed lines) to a shot without ECCD (solid lines).

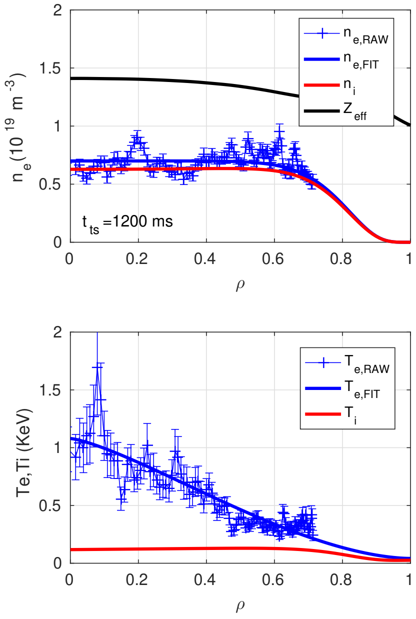

Figure 12. Electron/ion density and temperature profiles of the NBI+ECRH plasma. The profiles were measured at $t = 1200$ ms.

that two different levels of plasma current have on the observed AEs. Figure 11 illustrates the evolution of plasma parameters in both types of shots when ECH1 beam is used during the NBI phase. In this case, the power corresponding to each ECH beam is represented separately and their time traces overlap in the initial ECRH phase since they were operated at same power. As can be seen, independently of the value of $N_{\|}$, ECRH power produces a strong pump-out effect on the plasma density while central temperature increases from $T_e(0) \approx 400$ eV (NBI plasma only) to around 1.2 keV. Plasma densities and temperatures of electrons and ions obtained for the non-ECCD case are shown in figure 12. In this case – low density ECRH-like plasma – and following again [23], the ion temperature profile is taken proportional to the electron density profile. Although it is not shown here, very similar thermal plasma profiles are measured for the ECCD case since the heating source is barely modified. As expected, the main difference between shots with and without ECCD is the plasma current, which is stabilized at $t = 1200$ ms. While line density and central temperature remain basically the same, total plasma current decreases from $I_p \approx 1.0$ kA to $I_p \approx 0.3$ kA when ECCD is applied. This change in plasma current has a strong impact on the spectrum of detected perturbations, as is illustrated in the spectrograms shown in figures 13 and 14. A steady mode at 250 kHz appears while the low frequency activity is suppressed. The same experiment has been performed switching on ECH2 beam instead of ECH1. This beam is entering at a stellarator symmetric position in relation to ECH1 (see

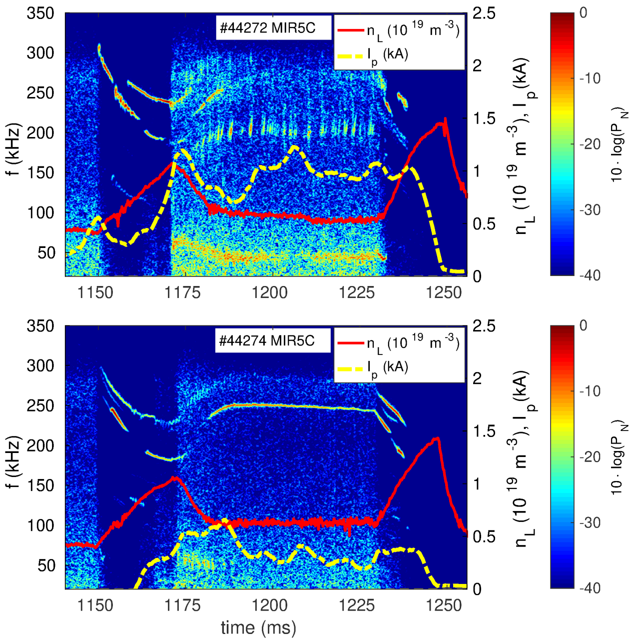

Figure 13. Impact of ECRH power (ECH1 beam) added during the NBI phase: without ECCD (top panel) and with on-axis ECCD launching the beam with $N_{\|} = 0.2$ (bottom panel). The main feature is the excitation of a steady mode with $f = 250$ kHz when ECCD is applied.

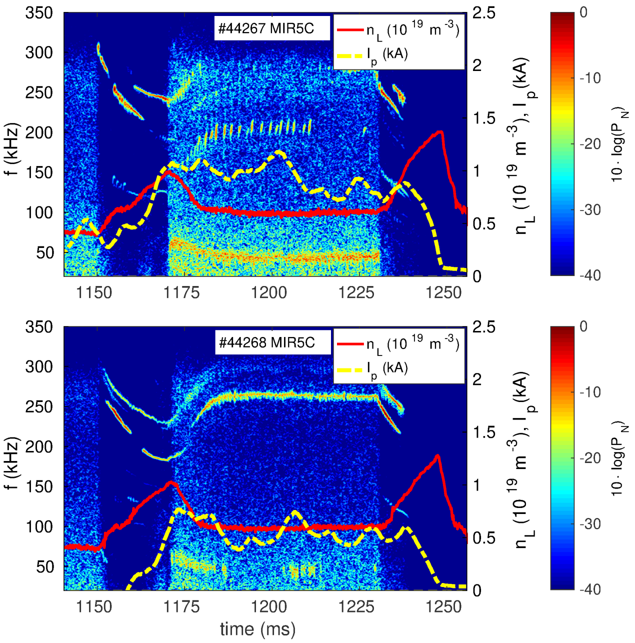

Figure 14. Same as in 13 but using now ECH2 beam instead of ECH1. Plasma current, temperature (not shown in the figures), density and magnetic fluctuations behave very similarly to the case depicted in figure 13.

figure 2) and its effect is very similar to the latter, as is shown in figure 14. In this case, the contribution of the counter-ECCD current is less pronounced and the same 250 kHz mode exhibits now a very slight chirping behavior. Low frequency activity is also suppressed. In contrast to the NBI case, no perturbations in plasma radiation are detected when ECRH (with or without ECCD) is applied. Note that in this case (see section 5) the NBI heating efficiency is extremely low.

5. NBI heating and fast ion pressure

A necessary input for mode stability analysis is the steady state fast ion pressure profile in both NBI and NBI+ECRH scenarios. Fast ion profiles resulting from the ionization of NBI neutrals and their subsequent slowing-down in the plasma have been calculated using the Montecarlo code FAFNER [24] with the thermal plasma profiles shown in figures 10 and 12 and the density of neutrals from recycling as obtained from EIRENE [25] for the given discharge conditions (plasma parameters, wall conditioning, puffing and monitored H_α light). The precise beam injection geometry is considered in the simulation including scraper losses. Fast ion densities (n_{fast}) and fast ion pressure profiles (β_{fast}) calculated with FAFNER are plotted in figure 15. Due to the relatively low plasma densities involved, for none of the cases is the NBI heating efficiency very high. For the NBI scenario – higher density and lower electron temperature – 58% of the port-through power (500 kW) is lost because of shine through. After considering charge exchange losses (17%) and particle orbit losses (7%) during slowing-down, the remaining coupled power goes to electrons (12%) and ions (6%). For the NBI+ECRH case with lower density and higher electron temperature, the NBI heating performance is even lower; percentage of shine through (54%) is very similar but charge exchange losses increase up to 30% leaving only 5% and 4% of the power for electrons and ions respectively after considering particle orbit losses (7%). All percentages are referred to the port-through total power.

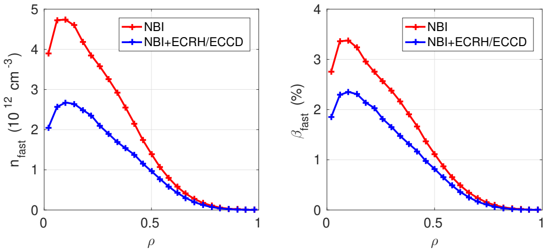

Figure 15. Fast ion density profiles (left) and β_{fast} profiles (right) calculated with FAFNER for the two relevant cases: NBI (red) and NBI+ECRH/ECCD (blue).

6. Plasma currents and impact on rotational transform profile

The three different scenarios described in sections 4.1 and 4.2 – NBI (1.5 kA), NBI+ECRH (1 kA) and NBI+ECRH with ECCD (0.3 kA) – show clearly different amplitudes of total plasma current. For the NBI and NBI+ECRH cases, the total current is a combination of NBCD and bootstrap contributions, which vary because of the changes in plasma profiles induced by ECRH. Furthermore, on-axis ECCD produces localized modifications of the current profile, affecting neither NBCD nor bootstrap since all plasma parameters remain very similar except for the EC driven current itself. The knowledge of the rotational transform profile $\iota(\rho)$ in each of the three cases is essential to understand changes on magnetic fluctuations and to compare the observed behavior to the theoretical predictions. Unfortunately, no ι measurements are available for these experiments and therefore, to take into account the impact of ι variations on the spectrum of shear Alfvén waves, the profile of each current source needs to be estimated. Thus, thermal plasma profiles have been first used to calculate the bootstrap current using DKES [26].

Then, the NBCD profile has been taken proportional to the fast ion density profile shown in figure 15 and finally, the TRAVIS ray tracing code [27] has been applied to estimate the ECCD current profile. Note that only the boostrap current result has been included without any modification while the calculated NBCD and ECCD profiles have been scaled so that the total integrated current that is obtained from adding the current density profiles of the different contributions is equal to the total measured plasma current. Figure 16 shows the result of such calculations for the three cases under study. We can now use the VMEC code [28] to calculate the corresponding equilibria and obtain the rotational transform profile for each case (see figure 17). Thermal plasma pressure ($\beta_{th}(0) \sim 0.3\%$) is disregarded in the equilibrium reconstruction and only the total current density is considered. Lower order rational values present in the rotational transform profiles determine the corresponding helicities, and therefore the range of m's and n's ($n/\iota_{max} < m < n/\iota_{min}$), that need to be included in the mode stability analysis presented in the next section.

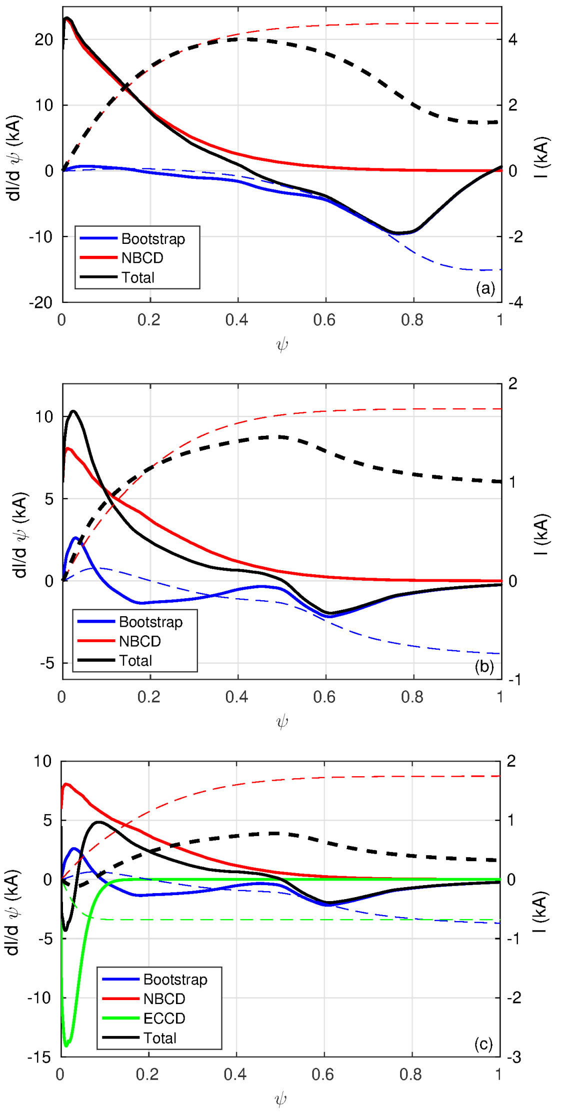

Figure 16. Radial profiles of the different contributions to the total plasma current profile (solid black lines) for the three studied cases: NBI (a), NBI+ECRH (b) and NBI+ECRH/ECCD (c). In all cases, the solid lines, blue for bootstrap, red for NBCD and green for ECCD, correspond to the calculated current profiles ($dI/d\psi\,(\psi)$), while the dashed lines ($I(\psi) \equiv \int_0^{\psi}[dI/d\psi']d\psi\prime$) represent their cumulative integral. Thus, the values of $I_p(\psi)$ at $\psi = 1$ correspond to the total stationary plasma current measured in each case.

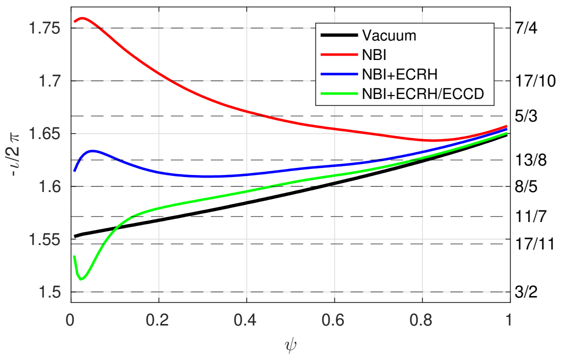

Figure 17. Rotational transform profiles calculated with VMEC and lower order rationals (right axis) for the studied cases. Vacuum iota profile is also shown.

Validating NBCD or ECCD calculations in the TJ-II stellarator is beyond the scope of the paper, however it is worth mentioning that taking the NBI induced current proportional to the fast ion density profile instead of the rigorous calculated NBCD profile is a sufficiently good approximation for our present purposes. Preliminary NBCD calculations in TJ-II [29] using the ASCOT code [30] to obtain the slowing-down distribution input was carried out for the same set of discharges. The result presented in [29] shows that current density profiles closely follow the radial distribution of fast ions although the current is overestimated since charge exchange losses were not taken into account in the ASCOT simulations. Similarly, the experimental validation of the bootstrap current calculations for TJ-II plasmas is still incomplete. The volume-integrated values routinely measured with Rogowsky coils for ECRH heated plasmas (without EC current drive) agree qualitatively with those estimated in [26]. For conditions similar to the NBI+ECRH plasma studied here, good quantitative agreement between the neoclassically-predicted ion contribution to the bootstrap current and the rotation profile of the fully ionized carbon [31] is found.

7. Mode stability analysis

The content of this section is devoted to the numerical analysis of the experimental results described in section 4. The structure of the Alfvén wave continuum has been calculated using STELLGAP [32] and the AEs stability has been studied by means of the FAR3d code [33–36]. The gyro-fluid code FAR3d solves the reduced linear resistive MHD equations together with the moment equations [37, 38] of the energetic ion density (n_{fast}) and parallel velocity ($v_{\|\text{fast}}$). The model reproduces the linear wave-particle resonance effects required for Landau damping/growth and the parallel momentum response of the thermal plasma required for coupling to the geodesic acoustic waves [39], as well as the effect of the helical couplings. FAR3d has been used in previous studies to model the experimental AEs and EPMs activity in LHD [40] and DIII-D [41] and to perform a parametric analysis of AEs destabilization in TJ-II [42].

STELLGAP		FAR3d (dyn.)		FAR3d (eq.)	
n	m	n	m	n	m
4	[1 – 8]	5	[2 – 4]	4	[0 – 5]
5	[1 – 10]	6	[3 – 5]	8	[0 – 5]
6	[2 – 12]	7	[3 – 6]	12	[2 – 7]
7	[2 – 14]	9	[4 – 7]	16	[5 – 10]
8	[3 – 16]	10	[5 – 8]	–	–
9	[3 – 18]	11	[5 – 9]	–	–
10	[4 – 20]	13	[6 – 10]	–	–
11	[4 – 21]	14	[7 – 11]	–	–
12	[5 – 23]	15	[7 – 11]	–	–
13	[5 – 25]	17	[9 – 13]	–	–
14	[6 – 27]	–	–	–	–
15	[6 – 29]	–	–	–	–
16	[7 – 31]	–	–	–	–
17	[7 – 33]	–	–	–	–

Table 1. Toroidal (n) and poloidal (m) mode numbers included in STELLGAP and FAR3d simulations. All poloidal mode numbers in the indicated range are included.

Table 1 indicates the values of toroidal (n) and poloidal (m) mode numbers included in STELLGAP simulations, as well as the values of the dynamic and equilibrium modes that have been considered in FAR3d. In this code, dynamic modes track the time evolution of the instability and equilibrium modes represent the plasma equilibrium and do not evolve in time. The closure of the kinetic moment equations breaks the MHD symmetry adding a phase with respect to the mode parity and thus mode parities must be included for all the dynamic variables. The representation of the several eigenfunctions in the FAR3d code is done in terms of sine and cosine components. More specifically, the real part of a general perturbation $\Phi(\rho, t)$ given by

$$\Phi(\rho, t) = \sum_{m,n} \phi_{m,n}(\rho) e^{i\beta},$$

with real frequency ω and phase $\beta \equiv \chi - \omega t$, where $\chi \equiv m\vartheta + n\varphi$ and $\phi_{m,n}(\rho)$ is the complex amplitude of the n/m mode, can be written as

$$\begin{aligned}\Re(\Phi(\rho, t)) &= \sum_{m,n} \Re([\phi^R_{m,n}(\rho) + i\phi^I_{m,n}(\rho)]e^{i\beta}) \\ &= \sum_{m,n} (\hat{\phi}^c_{m,n}(\rho, t)\cos\chi + \hat{\phi}^s_{m,n}(\rho, t)\sin\chi).\end{aligned}$$

where we have defined the functions

$$\hat{\phi}^c_{m,n}(\rho, t) \equiv \phi^R_{m,n}(\rho)\cos\omega t + \phi^I_{m,n}(\rho)\sin\omega t$$
$$\hat{\phi}^s_{m,n}(\rho, t) \equiv \phi^R_{m,n}(\rho)\sin\omega t - \phi^I_{m,n}(\rho)\cos\omega t$$

Having in mind the definition of χ (with "+" sign) and also that $\iota\!\!\!-$ is negative, n and m numbers of the calculated modes are both positive for the frequencies of interest. The $n > 0$ modes are those aligned with the magnetic field line helicity while the $n < 0$ modes are relevant at much higher frequencies than the ones detected in experiments. While solving for the different perturbations, the code provides the two solutions $\hat{\phi}^c_{m,n}$ and $\hat{\phi}^s_{m,n}$. In figures 21, 25 and 26, where the radial profile of the dominant perturbations are presented, the label n/m_c is used to represent $\hat{\phi}^c_{m,n}$, i.e. the component with $\cos\chi$ while the label n/m_s is used to represent $\hat{\phi}^s_{m,n}$, which is the component with $\sin\chi$. It should be noted that to describe the energetic particle population, the FAR3d code uses a Maxwellian distribution function with its temperature given by the average energy of the fast ion slowing down distribution and thus, in contrast to the real beam-like distribution function, co- and counter injected particles are being considered in the calculations.

The shear Alfvén continuum spectrum calculated for the three cases under study is shown in Figure 18. Its structure differs between cases on account of the differences in iota profiles and thermal plasma parameters. Consistently with the estimation shown in figure 1, two helical gaps (HAE$_{21}$ and HAE$_{31}$) are identified. For instance, for the NBI+ECRH/ECCD case (figure 18(c)), the presence of the HAE$_{21}$ gap allows the helical coupling between modes with toroidal number $n = 9$ (pink line) and $n = 13$ (brown line) in the middle plasma region ($\rho \approx 0.4$), around 230 kHz. For the NBI case, a much wider TAE gap appears at higher frequencies ($f = 300 - 350$ kHz), as it is clearly seen in figure 18(a). The three mode families $n = 0, n = 1$ and $n = 2$, typical of an $N_f = 4$ device, are plotted together for sake of space. FAR3d simulations use the fast ion density profiles obtained from the FAFNER code (see figure 15). As mentioned above, the code cannot take into account

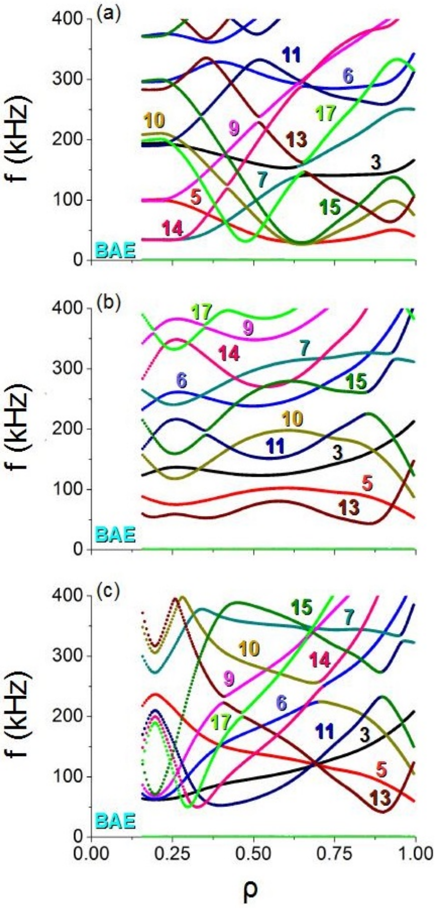

Figure 18. Alfvén wave continua calculated by the STELLGAP code for the cases (a) NBI, (b) NBI+ECRH and (c) NBI+ECRH/ECCD. The line color and index identify the toroidal mode number n. The frequency range of the BAE gap ($f < 50$ kHz) is also indicated.

the real distribution function created by the co-NBI beam. Therefore, FAR3d uses a Maxwellian distribution without radial energy dependency and average beam slowing-down temperature calculated with FAFNER: $T_{\text{fast}} = 10.0$ keV for the NBI case and $T_{\text{fast}} = 12.5$ keV for the NBI+ECRH/ECCD case. The magnetic Lundquist number S, defined as the ratio of the resistive time $\tau_R = a^2\mu_0/\eta_0$ to the Alfvén time $\tau_A = R_0\sqrt{\mu_0 m_i n_i(0)}/\bar{B}$, where $\bar{B}$ is the average magnetic field on-axis, varies between $S = 2\times10^6$ (for the highest collisionality NBI case) and $S = 8\times10^6$ (for the NBI+ECRH/ECCD cases). An average value $S = 5\times10^6$ is taken in the simulations.

It is also important to emphasize that although the VMEC equilibria used both in STELLGAP and FAR3d have been calculated including the plasma current to account for changes in $\iota\!\!\!-$, we have nevertheless disregarded the plasma pressure components when reconstructing the plasma equilibria. Since FAR3d simulations include necessarily the effect of the fast ions pressure profiles, the excited modes appear radially displaced and slightly shifted in frequency in respect to the gaps inside the continuum calculated by STELLGAP. This effect is noticeable in figures 21, 25 and 26, where FAR3d result is compared to the STELLGAP calculation.

In the following, the AE stability is analyzed for each case individually and the candidate modes that are found to be consistent in frequency with the observations will be labeled by their n/m ratio following the convention described above.

7.1. NBI

Figures 19 and 20 show different enlarged parts – between 150 and 250 kHz in figure 19 and between 80 and 120 kHz in figure 20 – of the magnetic perturbations spectrograms shown in figure 5. We focus the analysis on the time range for which the steady state density, temperature, $\iota\!\!\!-$ and fast ion profiles discussed in sections 4, 5 and 6 are assumed to be valid. As before, the spectrogram colors represent the single-side normalized mode power expressed in dB. This time, we have also added (right axis) the amplitude of the magnetic field perturbation perpendicular to the coil, $\delta B_s = \delta\mathbf{B}_s\cdot\hat{s}$. This quantity is given by

$$\delta B_s(t) = \frac{4C}{2\pi N_s f_m(t)}|\mathcal{STFT}(t,f)|_{f=f_m(t)} \tag{4}$$

where $\mathcal{STFT}(t,f)$ stands here for the short-time Fourier transform (or spectrogram) and $f_m(t)$ is the frequency at which the maximum amplitude in the spectrogram is observed. N_s is the number of samples in each short-time slice (1 ms) of the original signal and $C \equiv (1/\alpha N_t A_c) \approx 0.4\ \text{m}^{-2}$ is a factor associated to the signal amplification factor (α) and the coil geometry (N_t is the number of turns and A_c is the coil area). Three main instabilities clearly appear in the steady state part of the NBI phase, two of them around 180-200 kHz, labeled as `R1` and `R2` in figure 19 and a third one (`R3`) in figure 20. Detected amplitudes vary depending on the chosen coil. Now, figure 21 illustrates the result of the corresponding numerical simulations. The dominant instabilities consistent with the observations in terms of frequency are shown. According to the results presented in figures 21 (c) and (f), the 14/8 perturbation exhibits a frequency ($f = 179$ kHz) close to the measured frequency of instability `R1`. This 14/8 mode is identified as an energetic particle mode (EPM) because, in the simulation, a single poloidal mode number $m = 8$ is dominant and the mode radial extension is such that it intersects the continuum (see figure 21(c)). It is radially located above the HAE$_{21}$ gap at the position where $n = 10$ and $n = 14$ modes couple. The calculated dimensionless linear growth rate of this EPM mode is $\gamma\tau_A = 0.33$.

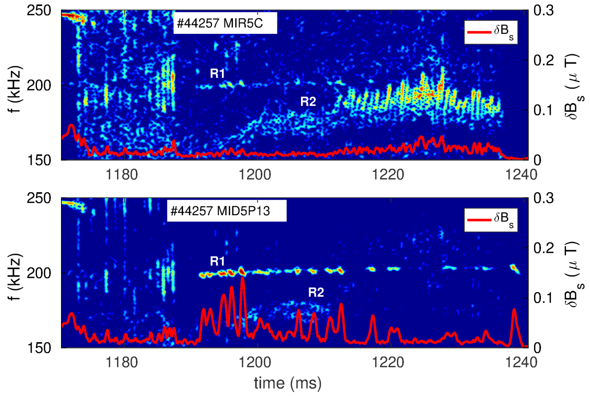

Figure 19. Magnetic fluctuations spectrograms in the 150-250 kHz range and mode amplitude $\delta B_s(t)$ for the NBI case measured by two different magnetic coils. Note that mode `R2` is barely seen by one of the coils (MID5P13).

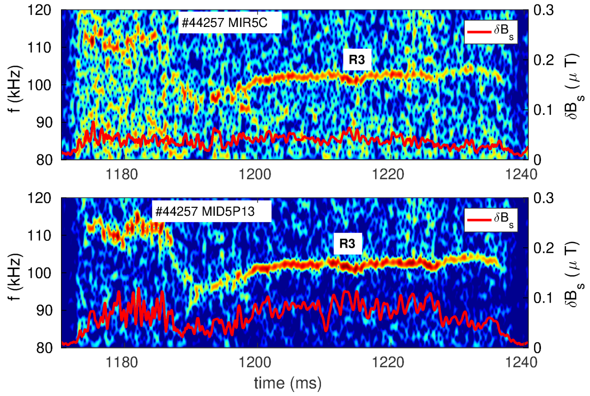

Figure 20. Magnetic fluctuations spectrogram in the 80-120 kHz range and mode amplitude $\delta B_s(t)$ for the NBI case measured by two different magnetic coils.

As for the chirping type instability `R2` clearly visible in one of the magnetic coils (MIR5C), FAR3d predicts the destabilization of a 17/10 perturbation (see figure 21(a)) whose calculated frequency ($f = 164$ kHz) is consistent with the average measured frequency of the `R2` mode ($f \approx 170-180$ kHz). The 17/10 perturbation is a helical Alfvén eigenmode (HAE) because it is triggered by the coupling of the $n = 13$ and $n = 17$ modes inside the helical HAE_{21} gap. For this case, $\gamma\tau_A = 0.37$. Another HAE mode within the frequency range of instability `R3` ($f \approx 100$ kHz) is found by FAR3d. This mode, also triggered within the HAE_{21} gap ($n = 3$ with $n = 7$ coupling), and shown in figure 21 (b) and (e) corresponds to a 7/4 HAE perturbation ($f = 107$ kHz) with $\gamma\tau_A = 0.31$. The calculated radial profile of the potential perturbation associated to this mode is roughly consistent with the HIBP measurements of the perturbed potential profile presented in figure 8 and with the radial extension of the perturbation as measured with radiation diagnostic (see figure 9). As an example, the 2D structure of the Φ potential perturbation linked to the 7/4 helicity induced mode is shown in figure 22.

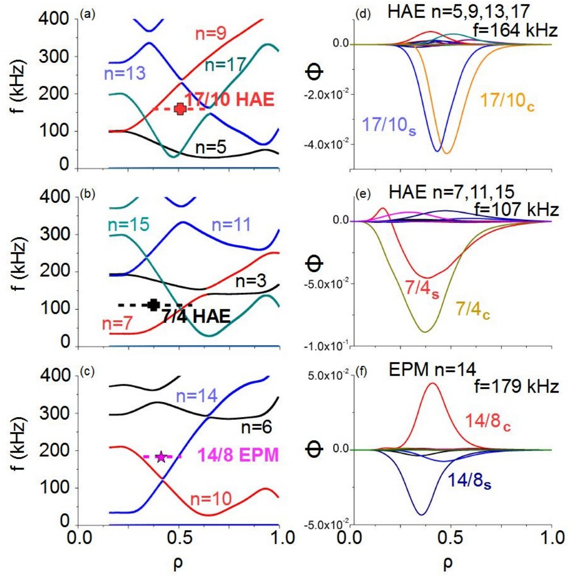

Figure 21. Alfvén waves continuum calculated with STELLGAP for the NBI case (a-c). The radial profile of the corresponding 17/10, 7/4 and 14/8 sine and cosine eigenfunctions found by FAR3d and consistent with the measured frequencies is also shown (d-f). For comparison, the frequency and the radial extension of the modes is indicated in the Alfvén continuum plots obtained with STELLGAP. As was explained in the text, n/m_c and n/m_s label the amplitudes of the $\cos(m\vartheta+n\varphi)$ and $\sin(m\vartheta+n\varphi)$ components. The calculation was performed with plasma profiles measured (and calculated in the case of $\iota\!\!\!-$) at t=1200 ms.

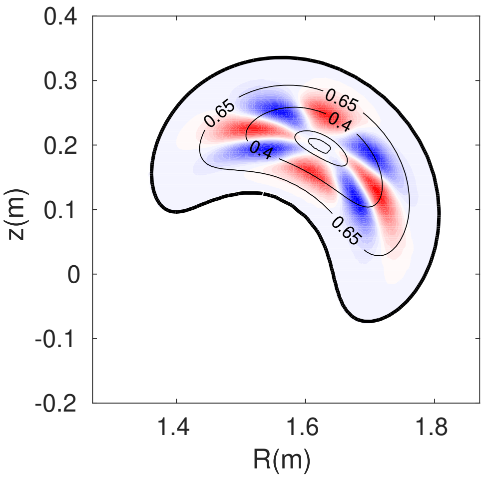

Figure 22. 2D plot of the $n = 7, m = 4$ potential perturbation calculated with FAR3d. The contour lines corresponding to $\rho = 0.4$ and $\rho = 0.65$ are also plotted.

7.2. NBI+ECRH and NBI+ECRH/ECCD

As was discussed in section 4, the main difference in plasma parameters between the cases in which ECRH is applied is the plasma current. Even though the stability analysis has been performed with experimental $(n_e(\rho), T_e(\rho), n_i(\rho))$ and calculated $(n_{\rm fast}(\rho), \iota\!\!\!{-}(\rho))$ steady state profiles taken at $t = 1200$ ms, the inspection of the time evolution of modes frequencies during the whole discharge provides very useful information. Figures 23 and 24 show the AEs activity, already presented in section 4.2, restricted now to the high frequency range, for the cases without and with ECCD driven by the ECH1 or the ECH2 beam.

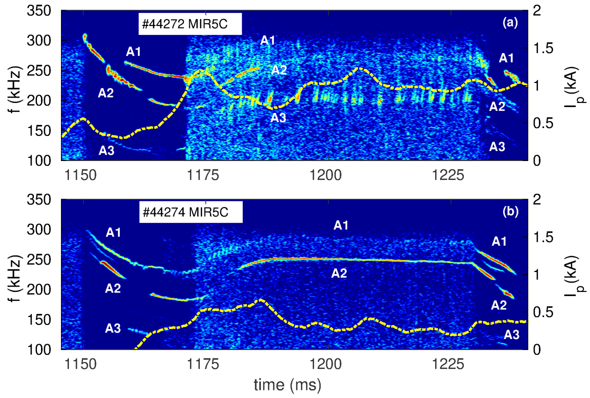

Figure 23. Magnetic fluctuations spectrogram without (a) and with ECCD (b) during the ECRH phase. In this case ECH1 beam was used to heat and then add EC current.

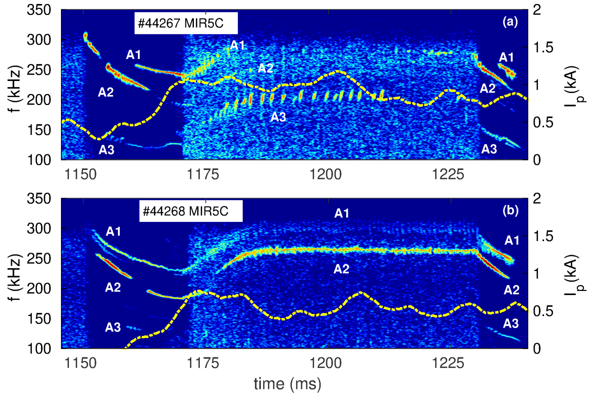

Figure 24. Same as figure 23 but using now ECH2 beam to heat and then add EC current by performing oblique launching.

Three main instabilities, labeled as `A1, A2` and `A3`, are present in all cases, with more or less amplitude and different behavior depending on the ECH beam used to drive the current. All three show very similar behavior during the phases without ECRH (1150 ms $<$ t $<$ 1170 ms) and t $>$ 1230 ms. Without ECCD, only the `A3` instability, very faint during the NBI phase, clearly survives during the ECRH phase, showing a more or less regular bursting behavior. `A1` and `A2` are barely detected after $t > 1185$ ms, although some hint of `A2` activity is detected at the end of the ECRH phase. When ECCD is applied, `A3` is suppressed, independently of the used ECH beam and `A2` survives mostly through the whole duration of the discharge showing a steady state behavior, particularly sharp in frequency if ECH1 beam is used. A very faint `A1` bursting activity is also observed in the cases with ECCD.

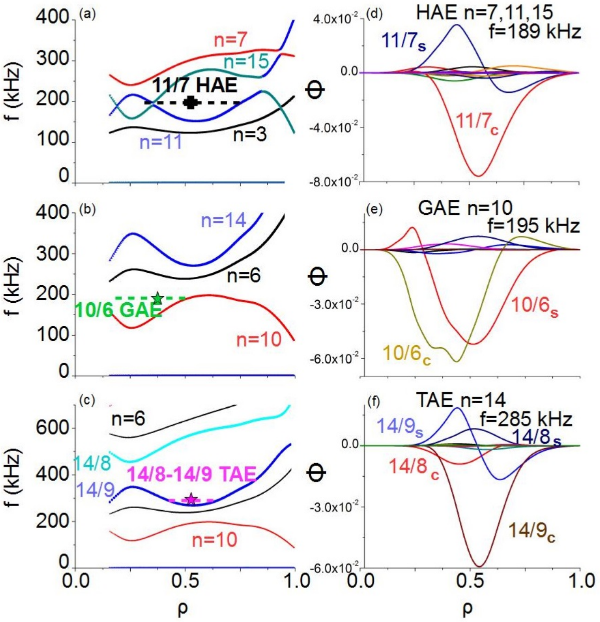

Figure 25. Alfvén waves continuum calculated with STELLGAP for the NBI+ECRH case (a-c). The radial profile of the corresponding 11/7, 10/6 and $14/8 - 14/9$ eigenfunctions is also shown (d-f). As before, the frequency and the radial extension of the modes is indicated in the Alfvén continuum plots obtained with STELLGAP. The calculation was performed with plasma profiles taken at t=1200 ms.

The numerical simulation for the case without ECCD makes appear two different instabilities with same linear growth rate ($\gamma\tau_A = 0.21$) and frequencies consistent with the frequency of the `A3` mode; an 11/7 HAE with f = 189 kHz, destabilized in the HAE$_{21}$ gap shown in figure 25(a) and a 10/6 GAE with f = 195 kHz, triggered at the radial location where the local minimum of the n = 10 BAE gap is found (figure 25(b)). In addition, also for the case without ECCD, the simulations predict the destabilization of $14/8 - 14/9$ perturbation (f = 285 kHz and $\gamma\tau_A$ = 0.19) which is shown in figures 25(e) and (f). The $14/8 - 14/9$ is a TAE mode because two modes with same n and successive poloidal mode numbers (m and $m{+}1$) are coupled. The perturbation is triggered inside the TAE gap shown in figure 25(e). Instability `A1`, which would be the most suitable candidate for this prediction shows a very faint amplitude and reaches $f \approx 290 - 300$ kHz before it disappears at $t = 1185$ ms.

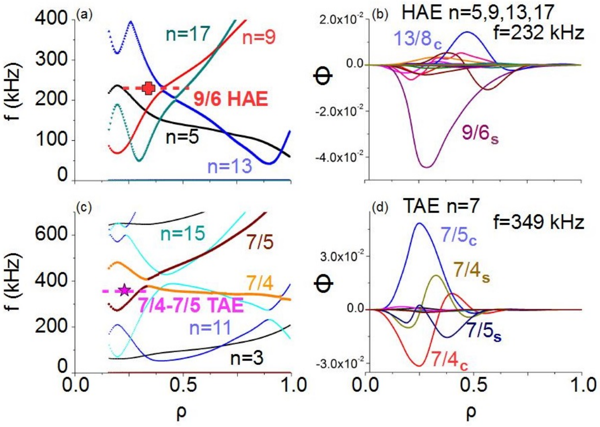

Figure 26. (a) Alfven gap location and (b) eigenfunction of the 9/6 HAE for the NBI+ECRH/ECCD case. Again, the result is obtained for t=1200 ms.

Finally, the results of FAR3d and STELLGAP simulations for the ECCD case are shown in figure 26. A 9/6 HAE perturbation (coupled with 13/8) with $f =$ 232 kHz and $\gamma\tau_A = 0.20$ is destabilized in the HAE_{21} gap and seems to be consistent with the frequency range of the instability `A2` shown in figure 23(b). Moreover, a higher frequency $7/4 - 7/5$ TAE ($f = 349$ kHz and $\gamma\tau_A = 0.20$) also arises in the simulations. However, the very faint chirping instability `A1`, which is shown in figure 28, being the one observed with the higher frequency, is still 50 kHz below predictions. Note that in this case the amplitude of fluctuations is one order of magnitude lower compared with `A2`. Figures 27 and 28 shows enlarged views of instabilities `A1` and `A2` and their amplitude. Amplitude of `A1` is one order of magnitude lower.

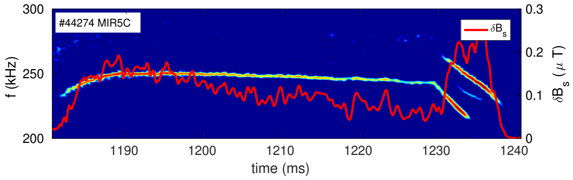

Figure 27. Magnetic fluctuations spectrogram in the 200-300 kHz range, corresponding to the `A2` instability shown in figure 23(b). Mode amplitude δB_s is also plotted.

The FAR3d simulations also identify some GAEs with $f < 160$ kHz and TAEs with $f > 350$ kHz which do not correspond to any instability observed in the experiments even though their growth rate is similar to the rates of those modes that match the experimental observations. Here it is important to remind that while FAR3d is considering a Maxwellian distribution, i.e. co and counter ions of equal energy, the experiments have been carried out only with co-injected ions coming from one single neutral beam injector. Actually, experiments performed with NBI2, whose analysis is beyond the scope of this paper, show that several AEs are also excited. FAR3d is very likely capturing this behavior although a rigorous calculation should consider the opposite (negative) current induced by NBI2. Another possible reason for this discrepancy is caused by the underestimation of the continuum damping effect on the GAEs with $f < 160$ kHz and the lack of the finite Larmor radius damping effect on the TAEs with $f > 350$ kHz. Both damping effects would contribute to stabilize these modes in the experiment.

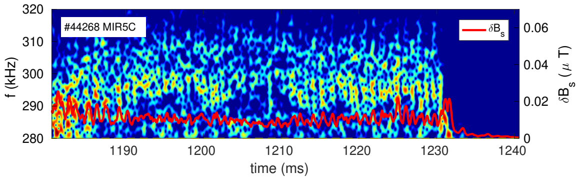

Figure 28. Magnetic fluctuations spectrogram in the 280-320 kHz range, corresponding to the faint `A1` instability shown in figure 24(b). Mode amplitude δB_s is also plotted.

7.3. Dependence of mode frequency on ECRH power

Taking the NBI+ECRH/ECCD scenario as a starting point (see figure 11), the impact of on-axis ECH power on the steady 9/6 helical mode shown in figure 27 is investigated using a 20 ms, 250 kW pulse of ECH2 starting at $t = 1200$ ms. Figure 29 shows three discharges obtained using the same settings. While they are very reproducible in terms of line density and central temperature, they show different uncontrolled time evolution of the plasma current. Within the measurement accuracy, adding ECH2 on-axis power no longer modifies the line density, as is shown in figure 29(a) but it still seems to have a very slight impact on the density profile (see figure 31(a)). Looking at the 9/6 mode frequency evolution shown in figure 30 we may immediately establish a correlation between mode frequency and changes in plasma temperature/density and also between mode amplitude and total plasma current. In all cases, mode frequency increases about 20 kHz when ECH power is applied while its amplitude decreases as plasma current becomes zero. Three different reference times (t_1, t_2 and t_3) indicating approximately the time for which the total measured plasma current is zero, are shown in figure 29 and for comparison with the mode behavior, also in figure 30.

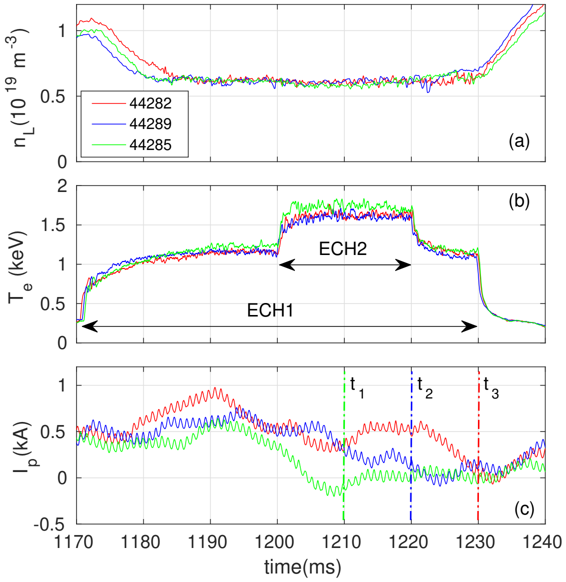

Figure 29. Time evolution of line density (a), central electron temperature (b) and plasma current (c) in three shots with same initial settings. The ECH1/ECH2 heating scheme during the NBI phase is indicated in (b). Reference times (t_1, t_2 and t_3) roughly indicate the times for which $I_p \approx 0$.

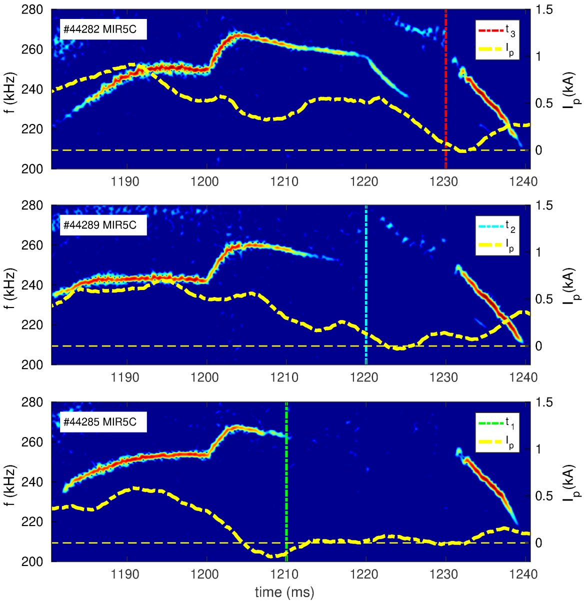

Figure 30. Dependence of mode frequency and amplitude on plasma temperature and current (yellow dashed line). Reference times t_1, t_2 and t_3 are indicated for comparison using the same color code defined in figure 29. At t=1230, ECRH power is switched-off and typical mode characteristic of NBI1-phase is recovered.

Even though the changes in local plasma density shown in figure 31 seem negligible, the amplitude of the errors bars mask variations that can account for the observed excursion in frequency. In principle, increments of Δf in mode frequency due to a reduction in local plasma density around the radial mode location can be roughly estimated using the simple square root dependence of the mode frequency on the ion density ($f \sim 1/\sqrt{n_i}$ and $n_i \simeq n_e$). Taking this approximation, we may evaluate the change in local ion density related to a Δf variation as $\Delta n_i \simeq n_i(f^2/(\Delta f^2 + f^2) - 1)$ and thus, increments of $\Delta f \simeq 20$ kHz in the 250 kHz range need $\Delta n_i/n_i \simeq -0.15$, that is, a 15% reduction in local density. According to this approximation, a maximum reduction of only 7% (from $n_e \simeq 0.75$ to $n_e \simeq 0.7$ at $\rho \approx 0.25$) can be inferred from the measured profiles shown in figure 31(a) and therefore either the previous approximation is too simple or the effect of temperature, whose changes are illustrated in figure 31(b), needs also to be taken into account to explain frequency variations. Actually, both density and thermal temperature effects may be analyzed with FAR3d and STELLGAP for a wide range of density and temperature variations. Figure 32 shows the dependence of normalized linear growth rate and frequency of the 9/6 HAE mode on the central plasma density at constant temperature ($T_e(0) \approx 1.2$ keV). The FAR3d simulation not only includes the effect of the ion density on the gap position but also the effect on the wave-particle resonance, that is now different since the Alfvén velocity has changed. The combined effects makes the calculated shift in frequency stronger than the one obtained considering only the simple $f \sim 1/\sqrt{n_i}$ approximation. FAR3d calculation shows also a non smooth variation of the linear growth rate as density increases which cannot be validated with the experimental observations presented here. A possible explanation for this effect would be the 9/6 mode attenuation together with the amplification of the 13/8 helically coupled mode as the density increases, thus

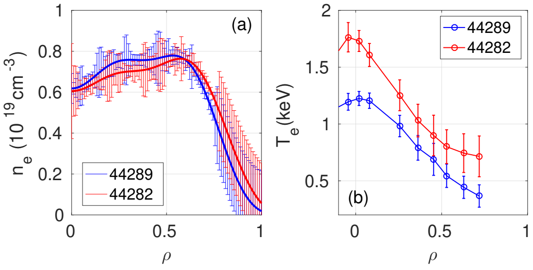

Figure 31. Density (a) and temperature (b) profiles measured at $t = 1190$ ms in shot 44289 (blue solid lines), before switching-on ECH2 beam, and at $t = 1210$ ms in shot 44282 (red solid lines) after switching-on ECH2.

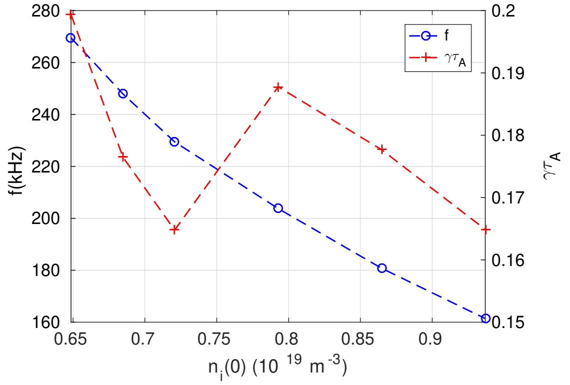

Figure 32. 9/6 HAE growth rate (dashed red line) and frequency (dashed blue line) for different central ion densities.

contributing to the increased growth rate while keeping consistency with the predicted smooth behavior in frequency. Although the simulations for variable densities at constant temperature predicts frequency variations more in accordance with the experimental results we must also take into account the impact of plasma temperature on mode frequency. A temperature increase implies a decrease of the plasma resistivity, which has a stabilizing effect, but also implies an increase of β_{fast}, which enhances the mode drive. A rise in temperature also increases the pressure of the thermal plasma, which results in a stabilizing (or destabilizing) effect if the continuum damping is enhanced (or weakened). Figure 33 shows the impact that variations in thermal temperature have on the growth rate and frequency of the 9/6 HAE mode as predicted by FAR3d. The central temperature is varied from $T_e(0) = 0.75$ to 1.75 keV in steps of 0.25 keV while thermal plasma density profile is kept constant at $n_e(0) \approx 0.75 \times 10^{19}$ m^{-3}. For an increment of central temperature similar to the one observed experimentally, that is, from $T_e(0) \simeq 1.25$ keV to $T_e(0) \simeq 1.75$ keV (see figure 31(b)), FAR3d predicts around 7 kHz increase in frequency. The combined impact on the mode frequency of lowering the density and increasing the temperature is calculated using the density and temperature profiles measured in the ECH2 phase (red lines in figure 31).The result is shown in figure 34. Comparing this result with the one shown in figure 26 we can see that the 9/6 HAE is still the dominant mode and that it has increased its frequency by an amount $\Delta f = 16$ kHz, which agrees reasonably with the frequency increment observed in figure 30. The effect of increasing the temperature on the fast-ion density profiles calculated with FAFNER and on the rotational transform profile due to current density redistribution have been disregarded.

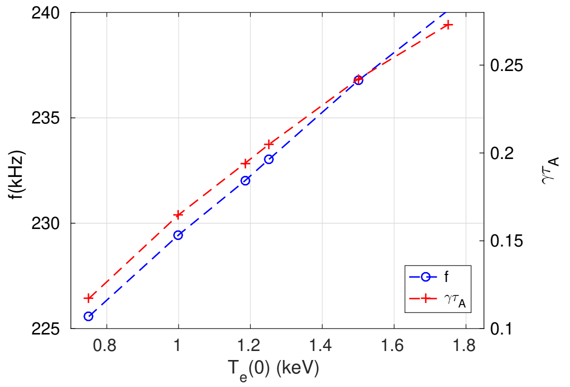

Figure 33. 9/6 HAE growth rate (dashed red line) and frequency (dashed blue line) for different central electron temperatures.

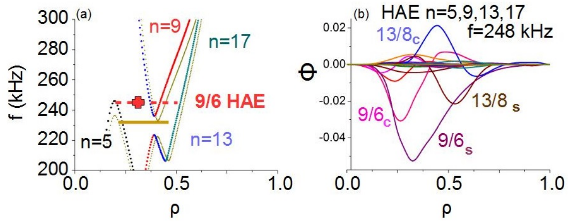

Figure 34. Effect of ECH2 power on the location of the HAE$_{21}$ Alfvén gap (a) and the 9/6 HAE eigenfunctions. Mode frequency is now 16 kHz higher.

8. Conclusions

We draw the following conclusions:

- NBI-driven Alfvén Eigenmodes experiments in the TJ-II stellarator show that a small amount of plasma current considerably modifies the spectrum of the observed magnetic field and plasma potential perturbations. This is consistent with the changes induced in the theoretical shear Alfvén spectrum when the impact of the plasma current on the rotational transform is evaluated. Using different VMEC equilibria with estimated current density profiles calculated in different scenarios allows us to evaluate these changes by means of the STELLGAP code.
- The effect of on-axis counter-ECCD can be easily isolated from the NBCD and bootstrap current contributions since modifying the injection angle of the ECH beams to induce current barely changes the power deposition profile and therefore produces negligible impact on NBI efficiency and plasma pressure. In this sense, ECCD is the most efficient actuator for control of AEs in TJ-II. Effect of co-ECCD remains to be investigated.

- Destabilization of several types of Alfvén Eigenmodes (GAEs, HAEs and possibly TAEs) and Energetic Particle Modes (EPMs) whose frequency is consistent with the frequency of the observed perturbations is successfully predicted by the FAR3d code. Moreover, the experimental dependence of mode frequency on the changes in plasma temperature and density induced by ECRH power are also in accordance with FAR3d estimations.

Even though the impact of plasma current on Alfvén Eigenmodes is clearly demonstrated when applying ECCD, all the current sources must be taken into account. Actually, having unbalanced NBI injection forces us to consider an estimation of the NBCD effect on the rotational transform profile as an indispensable condition to obtain reliable predictions. This is not needed in experiments with balanced NBI injection. Bootstrap current can neither be disregarded since its contribution is of the same order as the NBCD or ECCD. Although its impact on the rotational transform is lower due to its localization off-axis, knowing its integrated value is mandatory to impose the normalization of the theoretical current to the total measured plasma current.

Despite the inaccuracies related to the current density estimation (and therefore to the equilibrium configuration), FAR3d predictions show reasonable agreement with experimental results in all the scenarios studied. The TJ-II stellarator results presented here contribute to the experimental validation of the FAR3d code in 3D non-axisymmetric systems. Comparison of theoretical predictions with observations has already been carried out in other stellarators and presented in references [40, 43]. The characteristics of the MHD model implemented in the code, specially oriented towards computational efficiency, makes it an appropriate candidate for stellarator design optimization.

Acknowledgements

This work has been carried out within the framework of the EUROfusion Consortium and has received funding from the Euratom research and training programme 2014-2018 and 2019-2020 under grant agreement No 633053. The views and opinions expressed herein do not necessarily reflect those of the European Commission. The work was partially funded by the EUROfusion Enabling Research programme under project number ER-WP14-ER-01 and the Spanish Ministry of Science and Innovation under contract number FIS2017-88892-P. The work of the Kurchatov team was funded by the Russian Science Foundation under Project 19-12-00312 and the work of A. V. Melnikov was partly supported by the Competitiveness program of NRNU MEPhI. The authors also want to express their gratitude to Nikolai Marushchenko for his support with TRAVIS code.

References

[1] E.D. Fredrickson, G. Taylor, N. Bertelli, D.S. Darrow, N. Gorelenkov, G. Kramer, D. Liu, N.A. Crocker, S. Kubota, and R. White. Suppression of energetic particle driven instabilities with HHFW heating. *Nuclear Fusion*, 55(1):013012, 2014.

[2] M.A. Van Zeeland, W.W. Heidbrink, S.E. Sharapov, D. Spong, A. Cappa, Xi Chen, C. Collins, M. García-Muñoz, N.N. Gorelenkov, G.J. Kramer, P. Lauber, Z. Lin, and C. Petty. Electron cyclotron heating can drastically alter reversed shear alfvén eigenmode activity in DIII-D through finite pressure effects. *Nuclear Fusion*, 56(11):112007, 2016.

[3] D.C. Pace, C.S. Collins, B. Crowley, B.A. Grierson, W.W. Heidbrink, C. Pawley, J. Rauch, J.T. Scoville, M.A. Van Zeeland, and Y.B. Zhu and. Control of power, torque, and instability drive using in-shot variable neutral beam energy in tokamaks. *Nuclear Fusion*, 57(1):014001, 2016.

[4] S E Sharapov, M Garcia-Munoz, M A Van Zeeland, B Bobkov, I G J Classen, J Ferreira, A Figueiredo, M Fitzgerald, J Galdon-Quiroga, D Gallart, B Geiger, J Gonzalez-Martin, T Johnson, P Lauber, M Mantsinen, F Nabais, V Nikolaeva, M Rodriguez-Ramos, L Sanchis-Sanchez, P A Schneider, A Snicker, and P Vallejos and. The effects of electron cyclotron heating and current drive on toroidal alfvén eigenmodes in tokamak plasmas. *Plasma Physics and Controlled Fusion*, 60(1):014026, 2017.

[5] E.D. Fredrickson, E.V. Belova, N.N. Gorelenkov, M. Podestà, R.E. Bell, N.A. Crocker, A. Diallo, and B.P. LeBlanc and. Global alfvén eigenmode scaling and suppression: experiment and theory. *Nuclear Fusion*, 58(8):082022, 2018.

[6] K. Nagaoka, T. Ido, E. Ascasíbar, T. Estrada, S. Yamamoto, A.V. Melnikov, A. Cappa, C. Hidalgo, M.A. Pedrosa, B.Ph. van Milligen, I. Pastor, M. Liniers, M.A. Ochando, A. Shimizu, L.G. Eliseev, S. Ohshima, K. Mukai, and Y. Takeiri and. Mitigation of NBI-driven alfvén eigenmodes by electron cyclotron heating in the TJ-II stellarator. *Nuclear Fusion*, 53(7):072004, 2013.

[7] S. Yamamoto, K. Nagasaki, S. Kobayashi, K. Nagaoka, A. Cappa, H. Okada, T. Minami, S. Kado, S. Ohshima, S. Konoshima, Y. Nakamura, A. Ishizawa, G.M. Weir, N. Kenmochi, Y. Ohtani, X. Lu, Y. Tawada, D. Kokubu, and T. Mizuuchi. Suppression of fast-ion-driven MHD instabilities by ECH/ECCD on heliotron j. *Nuclear Fusion*, 57(12):126065, 2017.

[8] S. Yamamoto, K. Nagasaki, K. Nagaoka, J. Varela, A. Cappa, E. Ascasibar, F. Castejon, J. M. Fontdecaba, J. M. García Regaña, A González, K Ida, A Ishizawa, M Isobe, S Kado, S Kobayashi, M Liniers, D. Lopez-Bruna, N. B. Marushchenko, F. Medina, A. V Melnikov, T Minami, T Mizuuchi, Y Nakamura, M A Ochando, K Ogawa, S Ohshima, H Okada, M Osakabe, M Sanders, J L Velasco, G M Weir, and M Yoshinuma. Effect of ECH/ECCD on energetic-particle-driven MHD modes in helical plasmas. *Nuclear Fusion*, 2020.

[9] M Garcia-Munoz, S E Sharapov, M A Van Zeeland, E Ascasibar, A Cappa, L Chen, J Ferreira, J Galdon-Quiroga, B Geiger, J Gonzalez-Martin, W W Heidbrink, T Johnson, Ph Lauber, M Mantsinen, A V Melnikov, F Nabais, J F Rivero-Rodriguez, L Sanchis-Sanchez, P Schneider, J Stober, W Suttrop, Y Todo, P Vallejos,

and F Zonca and. Active control of alfvén eigenmodes in magnetically confined toroidal plasmas. *Plasma Physics and Controlled Fusion*, 61(5):054007, 2019.

[10] R. Jiménez-Gómez, A. Könies, E. Ascasíbar, F. Castejón, T. Estrada, L. G. Eliseev, A. V. Melnikov, J.A. Jiménez, D. G. Pretty, D. Jiménez-Rey, M.A. Pedrosa, A. de Bustos, and S. Yamamoto. Alfvén eigenmodes measured in the TJ-II stellarator. *Nuclear Fusion*, 51(3):033001, 2011.

[11] A.V. Melnikov, L.G. Eliseev, R. Jiménez-Gómez, E. Ascasibar, C. Hidalgo, A.A. Chmyga, A.D. Komarov, A.S. Kozachok, I.A. Krasilnikov, S.M. Khrebtov, L.I. Krupnik, M. Liniers, S.E. Lysenko, V.A. Mavrin, J.L. de Pablos, M.A. Pedrosa, S.V. Perfilov, M.V. Ufimtsev, T. Ido, K. Nagaoka, S. Yamamoto, Yu.I. Taschev, A.I. Zhezhera, and A.I. Smolyakov. Internal measurements of alfvén eigenmodes with heavy ion beam probing in toroidal plasmas. *Nuclear Fusion*, 50(8):084023, 2010.

[12] B.J. Sun, M.A. Ochando, and D. López-Bruna. Alfvén eigenmodes including magnetic island effects in the TJ-II stellarator. *Nuclear Fusion*, 55(9):093023, 2015.

[13] A.V. Melnikov, M. Ochando, E. Ascasibar, F. Castejon, A. Cappa, L.G. Eliseev, C. Hidalgo, L.I. Krupnik, A. Lopez-Fraguas, M. Liniers, S.E. Lysenko, J.L. de Pablos, S.V. Perfilov, S.E. Sharapov, D.A. Spong, J.A. Jimenez, M.V. Ufimtsev, B.N. Breizman, and and. Effect of magnetic configuration on frequency of NBI-driven alfvén modes in TJ-II. *Nuclear Fusion*, 54(12):123002, 2014.

[14] A.V. Melnikov, L.G. Eliseev, E. Ascasíbar, A. Cappa, F. Castejón, C. Hidalgo, T. Ido, J.A. Jiménez, A.S. Kozachek, L.I. Krupnik, M. Liniers, S.E. Lysenko, K. Nagaoka, J.L. de Pablos, A. Shimizu, S.E. Sharapov, M.V. Ufimtsev, and S. Yamamoto. Transition from chirping to steady NBI-driven alfvén modes caused by magnetic configuration variations in the TJ-II stellarator. *Nuclear Fusion*, 56(7):076001, 2016.

[15] G. Vlad, F. Zonca, and S. Briguglio. Dynamics of alfvén waves in tokamaks. *Rivista del Nuovo Cimento*, 22(7), 1999.

[16] Kolesnichenko Ya. I., Yamamoto S., Yamazaki K., Lutsenko V. V., Nakajima N., Narushima Y., Toi K., and Yakovenko Yu. V. Interplay of energetic ions and alfvén modes in helical plasmas. *Physics of Plasmas*, 11(1):158–170, 2004.

[17] Ya. I. Kolesnichenko, V. V. Lutsenko, H. Wobig, and V. Yakovenko. Alfvén instabilities driven by circulating ions in optimized stellarators and their possible consequences in a Helias reactor. *Physics of Plasmas*, 9(2):517–528, 2002.

[18] J. Guasp and M. Liniers. Fast ion behaviour for NBI scenarios in TJ-II. *Proceedings of the 10th Stellarator Workshop*, page 204, 1995.

[19] A. V. Melnikov. *Electric Potential in Toroidal Plasmas*. Springer Nature, 2019.

[20] D López-Bruna, Tsv Popov, and E de la Cal. Monte carlo estimates of edge particle sources in TJ-II plasmas. *Journal of Physics: Conference Series*, 700:012006, mar 2016.

[21] P. Helander and Dieter J. Sigmar. *Collisional transport in magnetized plasmas*. Cambridge Monographs on Plasma Physics, 2005.

[22] B. López-Miranda, B. Zurro, A. Baciero, and M. Martínez. A LIBS method for simultaneous monitoring of the impurities and the hydrogenic composition present in the wall of the TJ-II stellarator. *Review of Scientific Instruments*, 87(11):11D811, 2016.

[23] J. M. Fontdecaba, I. Pastor, J. Arévalo, J. Herranz, K. J. McCarthy, and G. Sánchez Burillo. Comparisons of electron temperature and density, and ion temperature profiles in the TJ-II stellarator. *Plasma and Fusion Research*, 5:S2085, 2010.

[24] J. Guasp and M. Liniers. Theoretical evaluations of neutral beam injection efficiency for the TJ-II helical-axis stellarator. *Fusion Science and Technology*, 24(3):251–258, 1993.

[25] D López-Bruna, Tsv Popov, and E de la Cal. Monte Carlo estimates of edge particle sources in TJ-II plasmas. *Journal of Physics: Conference Series*, 700:012006, 2016.

[26] J L Velasco, K Allmaier, A López-Fraguas, C D Beidler, H Maassberg, W Kernbichler, F Castejón, and J A Jiménez. Calculation of the bootstrap current profile for the TJ-II stellarator. *Plasma Physics and Controlled Fusion*, 53(11):115014, 2011.

[27] N.B. Marushchenko, Y. Turkin, and H. Maassberg. Ray-tracing code TRAVIS for ECR heating, EC current drive and ECE diagnostic. *Computer Physics Communications*, 185(1):165 – 176, 2014.

[28] S.P. Hirshman and J.C. Whitson. Steepest descent moment method for three - dimensional magnetohydrodynamic equilibria. *The Physics of Fluids*, 26(12):3553–3568, 1983.

[29] S. Mulas, J. Kontula, E. Olivares, Á. Cappa, D. López-Bruna, M.J. Mantsinen, M. Liniers, F. Castejón, E. Ascasíbar, T. Kurki-Suonio, I.L. Arbina, and TJ-II Team. Estimation of neutral beam current drive in the TJ-II stellarator. *22nd International Stellarator and Heliotron Workshop, Madison ,USA*, 2019.

[30] E. Hirvijoki, O. Asunta, T. Koskela, T. Kurki-Suonio, J. Miettunen, S. Sipilä, A. Snicker, and S. Äkäslompolo. ASCOT: Solving the kinetic equation of minority particle species in tokamak plasmas. *Computer Physics Communications*, 185(4):1310 – 1321, 2014.

[31] J. Arévalo, J.A. Alonso, K.J. McCarthy, and J.L. Velasco. Incompressibility of impurity flows in low density TJ-II plasmas and comparison with neoclassical theory. *Nuclear Fusion*, 53(2):023003, 2013.

[32] D. A. Spong, R. Sanchez, and A. Weller. Shear Alfvén continua in stellarators. *Physics of Plasmas*, 10(8):3217–3224, 2003.

[33] L. Garcia et al. *Proceedings of the 25th EPS International Conference, Prague, 1998, VOL. 22A, Part II, p.1757*, 1998.

[34] L.A Charlton, J.A Holmes, H.R Hicks, V.E Lynch, and B.A Carreras. Numerical calculations using the full MHD equations in toroidal geometry. *Journal of Computational Physics*, 63(1):107 – 129, 1986.

[35] L.A Charlton, J.A Holmes, V.E Lynch, B.A Carreras, and T.C Hender. Compressible linear and nonlinear resistive MHD calculations in toroidal geometry. *Journal of Computational Physics*, 86(2):270 – 293, 1990.

[36] J. Varela, D.A. Spong, and L. Garcia. Analysis of alfvén eigenmode destabilization by energetic particles in large helical device using a landau-closure model. *Nuclear Fusion*, 57(4):046018, 2017.

[37] D.A. Spong, B.A. Carreras, and C.L. Hedrick. Linearized gyrofluid model of the alpha destabilized toroidal Alfvén eigenmode with continuum damping effects. *Physics of Fluids B: Plasma Physics*, 4(10):3316–3328, 1992.

[38] C.L. Hedrick, J.N. Leboeuf, and D.A. Spong. Alpha–Alfven local dispersion relation and solutions. *Physics of Fluids B: Plasma Physics*, 4(12):3869–3882, 1992.

[39] D.A. Spong. Simulation of alfvén frequency cascade modes in reversed shear-discharges using a landau-closure model. *Nuclear Fusion*, 53(5):053008, 2013.

[40] J. Varela, W.A. Cooper, K. Nagaoka, K.Y. Watanabe, D.A. Spong, L. Garcia, A. Cappa, and A. Azegami. Effect of the tangential NBI current drive on the stability of pressure and energetic particle driven MHD modes in

LHD plasma. *Nuclear Fusion*, 60(2):026016, 2020.

[41] J. Varela, D.A. Spong, M. Murakami, L. Garcia, E. D'Azevedo, M.A. Van Zeeland, and S. Munaretto. Subdominant modes and optimization trends of DIII-D reverse magnetic shear configurations. *Nuclear Fusion*, 59(4):046017, 2019.

[42] J. Varela, D.A. Spong, and L. Garcia. Analysis of alfven eigenmodes destabilization by energetic particles in TJ-II using a landau-closure model. *Nuclear Fusion*, 57(12):126019, sep 2017.

[43] J. Varela, K. Nagasaki, K. Nagaoka, S. Yamamoto, K. Y. Watanabe, D. A. Spong, L. Garcia, A. Cappa, and A. Azegami. Modeling of the ECCD injection effect on the Heliotron-J and LHD plasma stability. *Nuclear Fusion*, 60(11):112015, 2020.